Intrinsic dependence of ice adhesion strength on surface roughness

Halar Memon, Junpeng Liu, Davide S.A. De Focatiis, Kwing-so Choi and Xianghui Hou*

Faculty of Engineering, University of Nottingham, University Park, Nottingham NG7 2RD, UK;

*Correspondence: xianghui.hou@nottingham.ac.uk

Abstract

The roles of surface roughness on icephobicity including ice adhesion strength have been long debated in icephobicity studies. However, the direct/systematic influence of surface roughness on ice adhesion strength while keeping other surface characteristics such as surface wettability and interfacial cavitation unchanged are seldom reported. In this paper, systematic reduction of ice adhesion strength with the decrease in surface roughness regardless of the surface wettability was demonstrated across all the studied material types, i.e. metallic surfaces and polymeric coatings with different surface wettability. In-situ icing observation studies indicated that the ice did not anchor on smooth metallic surfaces and polymeric coatings but anchored on rough surfaces including superhydrophobic coatings. Effect of surface wettability was argued against the ice adhesion strength based on our results and similar ice adhesion strength was found on materials having different wettability (i.e. hydrophilic and hydrophobic coatings, and surfaces having different contact angle hysteresis). On the contrary, the introduction of low surface energy chemicals (via deposition and/or functionalization) on the surface having similar surface roughness showed a direct reduction of ice adhesion strength. These results indicated the surface roughness is vital in achieving icephobic performance, however, the ultra-low ice adhesion strength could be achieved by the synergetic effect of low surface roughness and low interfacial cavitation (in line with the interfacial correlation factor).

25 Keywords: icephobicity, ice anchoring, surface roughness, icing

1 Introduction

Surface roughness plays a crucial role in imparting icephobicity and superhydrophobicity on a solid surface and superhydrophobicity is the synergetic result of low surface energy and rough asperities [1-4]. Air pockets generated by highly rough surface and low surface energy render the hydrophobicity of a surface in Cassie Baxter state, while high surface energy leads to a highly hydrophilic surface. Zou et al. [5] reported that the introduction of low surface energy thin films on the sandblasted surface raised the water contact angle from 37^{o} to 145^{o}. It is normally believed that surface roughness R_a from 100 nm to 100 μm was used to render the surface superhydrophobic for most of the cases [6-9].

Surface superhydrophobicity would minimize the water contact area to prevent the ice to form a strong bond (superhydrophobicity-induced icephobicity) [10-13] and this phenomenon favours the diversion to homogeneous nucleation or results in loosely formed ice. Another related study indicated that contact angle hysteresis (CAH) on superhydrophobic surface and strength of ice adhesion are significantly dependent on the ice-solid contact area [14]. However, this hypothesis has limited applications and is not applicable in the cases of (a) the micro-frost formation under high humidity conditions [15-20], (b) maintaining high receding angles at sub-zero temperature [21, 22], (c) mechanical interlocking between ice and highly complex rough asperities on the superhydrophobic surface [23-25], and (d) increased number of hydrogen bonds (water-solid) [26-29]. All these factors form the main hurdles in the deployment of the superhydrophobic surface in icephobic applications [30].

Surface texturing or patterning has also been argued for achieving icephobicity [31-33], via the superhydrophobicity-induced icephobicity [8, 15, 34, 35] and some promising results were reported in anti-icing applications (e.g. droplet freezing delays, etc.) [36, 37]. Mishchenko et al [9] manufactured surfaces with highly ordered nano-scaled roughness

using Bosch process on various substrates. They studied the surfaces with wettability, and reported ice accretion delay on hydrophilic, hydrophobic and superhydrophobic surfaces by a few seconds, approximately 1 minute and remarkable >10 minutes, respectively. Eberle et al [38] fabricated various hydrophobic and hydrophilic surfaces with different nano-scaled roughness with RMS ranging from 0.17 nm to 176 nm, and demonstrated approximately 25 hours of droplet freezing delays on surfaces with ultrasmooth Si surface. However, these extraordinary improvements on anti-icing performance did not directly contribute to de-icing (shear removal of ice) abilities in most of the work and the anti-icing studies were mainly conducted on superhydrophobic surfaces. In addition, it is important to note that these freezing delays were mainly observed under static testing conditions. For dynamic droplet impact at aircraft velocity, the effect of freezing delay may be limited.

It is reported that ice nucleation can be annihilated or immensely delayed by deploying surface with roughness close to or smaller than critical ice nuclei size (1.2 nm – 2 nm under supercooling) [37, 38]. The rate of ice nucleation over the surface depends on homogenous and heterogeneous nucleation barriers [39, 40]. It is important to control or minimize the heterogeneous nucleation rate, which is mainly influenced by foreign particles present in the water and on the surface, interfacial energies among the surface, and interaction of the liquid/solid and surface geometries. By favoring the homogenous nucleation, the need to control effective contact area as required by superhydrophobicity-induced icephobicity methods [41] could be eliminated. Previous studies have indicated the surface roughness (R_a) of less than 100 nm [37, 42, 43] is instrumental to induce anchor-free ice nucleation over the surfaces and the annihilation of ice nucleation may be possible on surfaces with roughness less than 10 nm [36, 38].

In our previous work [44], the anchoring mechanism on rough surfaces was observed and validated using in-situ water condensation and icing observation. The results indicated the

dependence of ice adhesion strength with surface morphology. However, it is essential to study the direct effect of surface roughness, while keeping other parameters such as surface wettability or interfacial cavitation unchanged. In this work, the systematic reduction of ice adhesion strength was demonstrated with the decrease of surface roughness regardless of surface wettability. Correlations with other surface characterises such as surface wettability and interfacial cavitation were also studied. Furthermore, in-situ de-icing observation validated the intrinsic dependence of ice adhesion strength on surface roughness. The findings indicated that the surface roughness is vital in achieving icephobic performance. Ultra-low ice adhesion strength could be achieved by the synergetic effects of low surface roughness and interfacial cavitation/surface energy.

2 Experimental

5 types of materials/coatings were used in this study and the surfaces were evaluated and compared based on static and dynamic water contact angles (WCAs) including advancing WCAs (AWCAs), receding WCAs (RWCAs) and contact angle hysteresis, surface roughness, and ice adhesion strength. The material types and coatings are summarized in table 1 and their properties are detailed in supplementary table S1.

2.1 Substrates and raw materials

Stainless steel 303 (SS 303) and aluminum 2024 (Al 2024-T4) plates with the size of 50 mm x 20 mm x 3 mm and 50 mm x 20 mm x 1 mm respectively were used. 1H,1H,2H,2H-Perfluorooctyltriethoxysilane (POTS) was procured from Fluorochem Ltd UK. Micro-polishing cloth and colloidal silica suspension were procured from Struers and MetPrep respectively. N, N-Dimethylformamide (DMF) was supplied by Sigma-Aldrich UK.

Two-part thermoset polyurethanes namely Vytaflex 40A (PU-1), Smooth-Cast Semi-Rigid Series 61D (PU-2), Smooth-Cast 320 70D (PU-3) and Smooth-Cast ONYX 80D (PU-4) were

procured from Smooth-on (USA), and thermoplastic polyurethane matrix Estane 54610 (TPU) in form of pellets was provided by Lubrizol (USA). Polydimethylsiloxane (PDMS) R-2180 was purchased from NuSil technology. Hexagonal Boron Nitride nanoparticles with a size of 70 nm (hBN NPs) were obtained from Lower Friction (Canada). Hydrophobic functionalized silicon dioxide nanoparticles AEROSIL R 9200 ($nSiO_2$) were purchased from Evonik UK. All the materials were used as received.

2.2 Preparation of coatings/surfaces

All aluminium and stainless steel plates were washed with ethanol and deionized water thrice and then dried using compressed air, prior to testing and further treatment.

The metallic plates were smoothened using grinding and polishing with a series of steps employing sandpapers having grits sizes of (i) 220 and 320, (ii) 400, 600 and 1 µm polishing cloths, and (iii) 0.25 µm (chemically induced) polishing cloths using Metprep colloidal silica suspension particles for samples (i) Al-S1/SS-S1, (ii) Al-S2/SS-S2 and (iii) Al-S3/SS-S3, respectively. Al-SB/SS-SB samples were roughened using a Guyson F1200 sandblaster system with Guyson 180-220 µm alumina particles and Al-fSB/SS-fSB samples were subsequently functionalized using POTS by employing chemical vapor deposition (CVD) method as reported elsewhere [45].

PU-1, PU-2, PU-3, and PU-4 resins were prepared using magnetic stirring at Part A : Part B ratios of 100:100, 100:93, 100:90 and 100:83 respectively. Then the resins were brush coated on the Al-AR substrates. PU-1 coatings were cured at room temperature (RT) for 16 hours and post-treated at 65 ^{o}C for 4 hours. PU-2 and PU-3 coatings were cured at 30 ^{o}C for 5 hours and post-treated at 65 ^{o}C for 4 hours. PU-4 coatings were cured 65 ^{o}C for 5 hours and post-treated at 121 ^{o}C for 4 hours.

Thermoplastic polyurethane (TPU) coatings were developed by dissolving 1 gram of TPU pellets in 1.5 ml of DMF and the coatings were applied using the dip-coating method. Hydrophobic functionalization of hBN NPs (TPU-f5) was performed in a solution containing 400 mg of hBN NPs in 400 ml ethanol and the solution was ultrasonically mixed for 1 hour. 3 ml of POTS were added in the solution and the hBN NPs were treated at 80 ºC for 120 under reflux. The resultant was separated using a centrifuge method and the hBN NPs were washed several times with ethanol and water. NPs were then overnight dried in an oven at 100 ºC. For TPU/hBNs coatings (TPU-5/5f/10/40/60/80), 2 grams of TPU pellets were dissolved in 3 ml of DMF on a magnetic stirrer at 60 ºC. TPU/hBNs coatings with 5/10/40/60/80 wt% of hBN NPs were dispersed in 1/1.5/3.0/4.0/5.0 ml DMF using ultrasonic mixing for one hour respectively. Magnetic stirring was then used to mix the solution in a single vial for 60 minutes, followed by 30 minutes of ultrasonic mixing. All TPU/hBNs coatings were fabricated using the dip-coating method.

For PDMS coatings, magnetic stirring was used to mix 1 gram of PDMS Part A and Part B (1:1) in 3 ml xylene for 3 hours. For PDMS/ nSiO_2 coatings (SHS-5/10/20/40), magnetic stirring was used to mix 1 gram of PDMS Part A and Part B in 1 ml xylene for 3 hours and ultrasonically dispersing 5/10/20/40 wt% of nano-SiO_2 in 2.5/3.0/3.5/4.0 ml of xylene, respectively. The formed nanoparticle dispersions were then mixed with the PDMS solution using magnetic stirring for one hour, followed by 30 minutes of ultrasonic mixing.

Chemat Technology spin-coater kW-4A was used to apply the PDMS/ nSiO_2 coatings on Al-AR samples at a rotation speed of 1500 RPM for one minute and the samples were dried and cured at 60 ºC for 60 minutes, and then 150 ºC for 150 minutes.

Table 1: List of sample types and their compositions

Sample types	Sample names	Surface / substrates	Surface treatment / coating	Description
Aluminium substrates	Al-AR	Al2024 T4	-	-
	Al-SB	Al2024 T4	Sandblasted	-
	Al-fSB	Al2024 T4	Sandblasted	POTS Functionalized
	Al-S1	Al2024 T4	Grinding	Grinded (600 grit)
	Al-S2	Al2024 T4	Polished	1 µm polishing cloth
	Al-S3	Al2024 T4	Polished	0.25 µm Silica particles
Stainless steel substrates	SS-AR	SS 303	-	-
	SS-SB	SS 303	Sandblasted	-
	SS-fSB	SS 303	Sandblasted	POTS Functionalized
	SS-S1	SS 303	Polished	Grinded (600 grit)
	SS-S2	SS 303	Polished	1 µm polishing cloth
	SS-S3	SS 303	Polished	0.25 µm Silica particles
Pristine polymers coatings	PU-1	Al2024 T4	PU	-
	PU-2	Al2024 T4	PU	-
	PU-3	Al2024 T4	PU	-
	PU-4	Al2024 T4	PU	-
Polymeric nanocomposite coatings	TPU	Al2024 T4	TPU	-
	TPU-5	Al2024 T4	TPU	hBN (5 wt%)
	TPU-f5	Al2024 T4	TPU	POTS Functionalized hBN (5 wt%)
	TPU-10	Al2024 T4	TPU	hBN (10 wt%)
	TPU-40	Al2024 T4	TPU	hBN (40 wt%)
	TPU-60	Al2024 T4	TPU	hBN (60 wt%)
	TPU-80	Al2024 T4	TPU	hBN (80 wt%)
Superhydrophobic coatings	PDMS	Al2024 T4	PDMS	-
	SHS-5	Al2024 T4	PDMS	$nSiO_2$ (5 wt%)
	SHS-10	Al2024 T4	PDMS	$nSiO_2$ (10 wt%)
	SHS-20	Al2024 T4	PDMS	$nSiO_2$ (20 wt%)
	SHS-40	Al2024 T4	PDMS	$nSiO_2$ (40 wt%)

145

2.3 Surface characterization

A Zeta-20 non-contact optical profiler was used to evaluate the surface roughness. The roughness values in this study were the averages of several measurements (minimum of 30 readings at least) and R_a was measured over a line stretching across the observed surface (348 µm x 261 µm). Shore hardness on the developed polymers was measured using a SAUTER durometer having shore hardness A and D scales. The durometer was attached to SAUTER test stands TI-AO and TI-D for shore hardness A and D scales, respectively. The hardness studied in this work was indicative of an average penetration (shore) value based on 10 readings of testing.

An FEI Quanta 650 ESEM (environmental scanning electron microscope) with controlled humidity and temperature was used to perform in-situ icing observations. In the in-situ icing study, the chamber humidity was raised above 90% RH to wet the surface and the temperature was dropped to sub-zero temperature (down to -5 ^{o}C) using a Peltier cooling plate to allow the ice growth over the surface. The system is capable of generating micro-level SEM images for water droplet condensation and icing study, and ice retracting behaviour on the surface was analyzed.

2.4 Evaluation of hydrophobicity and icephobicity

Sessile drop technique was used to measure water contact angles (WCAs) using an FTÅ200 goniometer and 5 µl of a controlled volume of water drop was analyzed. The dispense tip method was used to measure dynamic WCAs (advancing and receding angles) with 5 µl droplets. Advancing and receding WCAs were measured when the base area (contact) of the droplets was increasing or decreasing constantly. The flow rate of the water was kept constant at 1 µl/s and 5 consecutive values were measured to ascertain the dynamic WCAs

values. CAH was calculated from the difference between AWCAs and RWCAs. The tests were conducted at room temperature.

A MOOG G403-2053A servo motor was used to measure the ice adhesion strength tests via the centrifugal method and the test was performed in a Design Environmental Chamber (ALPHA 1550-40H) to simulate the freezing conditions. Ice was formed on top of the samples using silicone moulds filled by de-ionized water with controlled volume and the moulds were then flipped upside down and kept against gravity for overnight freezing at -10 ^{o}C. The samples with the formed ice were then mounted on a carbon fibre reinforced arm via screws and spun at a rotation speed up to 4500 rad/min at 30 rev/min/sec acceleration (3.14 radian/second^2). The ice adhesion test was conducted at a temperature of -10 ^{o}C.

The ice adhesion strength on the samples can be calculated by,

$$F = mr\omega^2 \quad (1)$$

Where ω is the rotational speed (rad/s) at ice removal, r is the rotor length and m is the mass of ice. Shear removal stress can be calculated by,

$$\tau_{ice} = {}^{F}/_{A} \quad (2)$$

Where A is the substrate/ice contact area and F is the centrifugal shearing force.

The centrifugal method to evaluate the ice adhesion strength in this work has previously been applied by many researchers [46-48] and a recent publication indicated its compatibility with the other widely used methods such as horizontal force transducer method [49]. However, for a dynamic test such as the centrifugal method, there is always a risk of inherent motion or shake during the sample mounting procedures [50], and we rectified it by developing multiple rods that could be directly used for ice accretion on the samples and then mounted on the

testing rig with minimal impact on the ice bonding. The obtained results closely correlated to in-situ study on surface ice retraction.

3 Results and discussion

3.1 Growth of ice on developed surfaces

Ice adhesion strength is dependent on various factors including surface variables, purity of water, and the growth of ice over surfaces (heterogeneous or heterogeneous-homogenous mixed formation of ice) [7, 51]). Previous studies (static type tests) suggested that the heterogeneous nucleation is accelerated if the interfacial correlation factor $f(m, R')$ is altered by increasing the effective area of contact or by changing the wettability of the surfaces. Interfacial correlation factor (i.e. probability of ice nucleation) is defined into two parameters i.e. m and R' [41]. m is defined as,

$$m = {(\gamma_{sf} - \gamma_{sc})}/{\gamma_{cf}} \approx cos\theta^0 \ (-1 \leq m \leq 1) \quad (3)$$

Where γ_{cf}, γ_{sc} and γ_{sf} are the interfacial energies between the crystal phase and the fluid phase, the substrate and the crystal phase, and the substrate and the fluid phase respectively, and θ^0 is the contact angle of the ice nucleus on the substrate. R' is defined as

$$R' = {R}/{R_c} \quad (4)$$

Where R is the radius of a flattened surface and R_c are the critical radius of the nuclei on the surface (at a specified temperature and nucleation condition). When $R \geq R_c \, sin\theta^0$, the contact angle (where θ^0 is the contact angle of the ice nucleus on the substrate) remains unchanged on the surface and when $R < R_c \, sin\theta^0$, the contact angle grows at a rate of $sin^{-1}\left({R}/{R_c}\right)$ as it is limited due to geometric restriction of the surface [41].

Thus the interfacial correlation factor is dependent on the radius of a surface to the critical radius of the surface (R') and the synergetic effect of the average binding affinity of water to the surface and interfacial free energies (water/ice-surface) (m). It is assumed that the introduction of low surface energy without changing surface roughness will not significantly prevent ice nucleation. Furthermore, our results also indicated that the surface roughness is a more dominating factor than the effective area and the wettability. In order to effectively validate our hypothesis on surface roughness, we developed a series of surfaces and altered their surface roughness while retaining the surface compositions.

3.2 Influence of surface roughness and wettability on ice adhesion strength

In this section, we developed a series of metallic substrates and polymeric coatings with different wettability. The coatings/substrates were carefully fabricated to control the surface roughness and the ice adhesion strength tests were performed on these surfaces.

3.2.1 Stainless steel surface

Ice adhesion strengths on stainless steel (SS) surfaces were shown in figure 1. Firstly, the ice adhesion strengths were in correlation with surface roughness and the lowest ice adhesion strength was recorded on SS-S3 samples at 22.2 ± 2 KPa. 33-fold reduction in surface roughness (from SS-SB to SS-S3) resulted in a 3-fold reduction in ice adhesion strength (i.e. adhesion reduction factor, ARF).

However, no significant reduction in ice adhesion strength was observed on SS-S2 and SS-S3, i.e. 25.4 ± 7 and 22.2 ± 2 KPa respectively. Report from the literature [52, 53] indicated a correlation (directly proportional) with the contact angle hysteresis (CAH) but such results were not observed on our SS substrates except for the SS-S2 and SS-S3 samples.

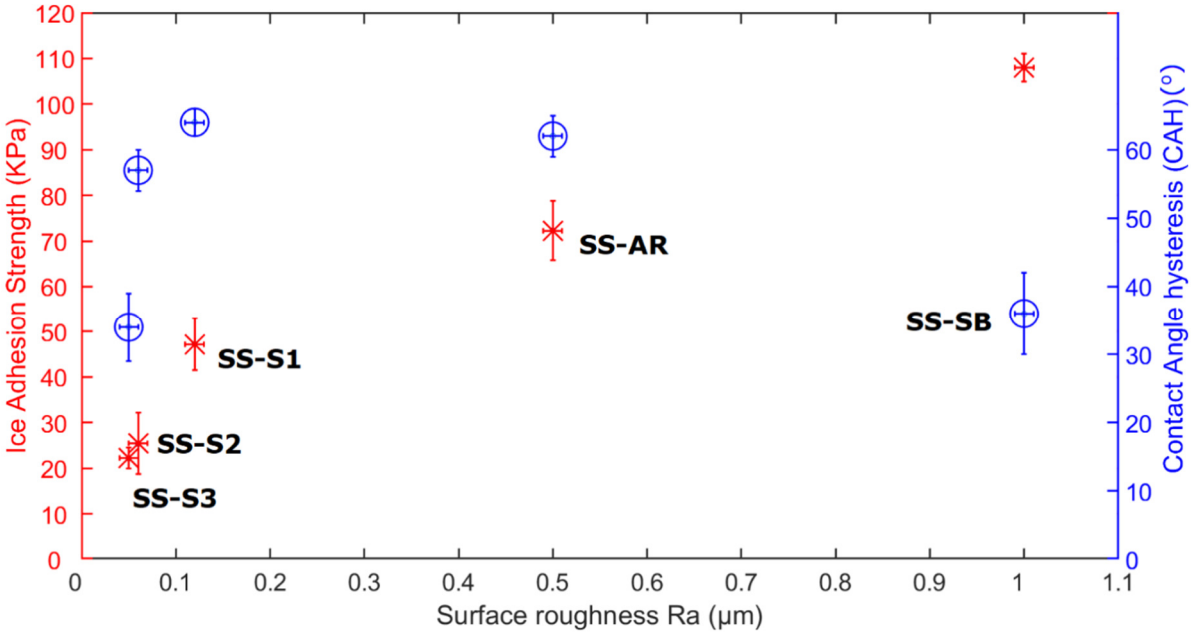

Figure 1: Ice adhesion strength on stainless steel substrates with different surface roughnesses.

234

235 **3.2.2 Aluminium surface**

236 Significant reduction in ice adhesion strength was observed on aluminium substrates in
237 comparison to SS substrates, as shown in figure S2 from the supplement. It is imperative to
238 mention that the surface roughness of Al substrates was reduced 24 times (from Al-SB to Al-
239 S3) as compared to a 33-fold roughness reduction on SS substrates. Ice adhesion strength was
240 reduced from 145.5 ± 3 KPa on Al-AR samples to 13.1 ± 1 KPa on Al-S3 samples i.e. 91%
241 deduction and ARF of 11. The decrease in ice adhesion strength observed on the metallic
242 samples was mainly achieved by altering just one surface parameter, i.e. surface roughness.

243 In comparison with SS substrates, a similar pattern of ice adhesion strength dependence on
244 surface roughness is noticed on Al substrates. Ice adhesion strength highly correlated with the
245 reduction of surface roughness when above 100 nm and smoothening of substrates with
246 roughness of less than 100 nm i.e. Al-S2 and Al-S3 (and SS- S2 and SS-S3 in section 3.2.1)
247 did not produce a significant change in ice adhesion strength. Interestingly, for the metal
248 substrates, CAH is demonstrating some correlation with ice adhesion strength until surface

roughness reaches ~0.5 µm and loses the correlation when the surface roughnes is higher than 0.5 µm. However, the value of 0.5 µm is not a rigid figure and the assumption is made based on the available results. Another considerable observation is that Al-S2 and Al-AR have similar CAHs but the ice adhesion strength varied by ~89% (reduction).

3.2.3 Polymeric surfaces

3.2.3.1 Pristine polymeric coatings

Polymeric nanocomposite showed a drastic change in ice adhesion strength with surface roughness and a similar pattern of ice adhesion strength dependence on surface roughness (in comparison with other coatings) was followed on polymeric surfaces i.e. PDMS, PU-1, PU-2, PU-3, and PU-4 coatings, as indicated in figure 2.

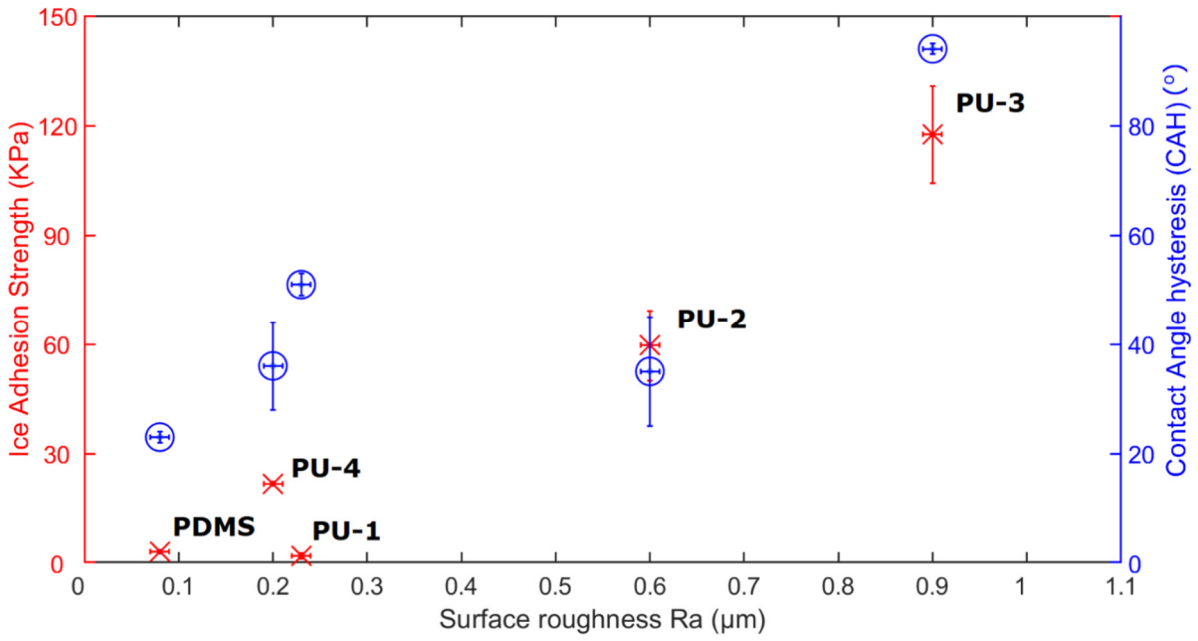

Figure 2: Ice adhesion strength on pristine polymeric coatings with different surface roughnesses.

Although the surface energy of the studied coatings might differ, the basic composition of PU-based coatings was assumingly the same. The highest ice adhesion was measured on PU-3 coatings at 117.6 ± 13.3 KPa and the lowest was 2 ± 0.8 KPa on PU-1 coatings.

Interestingly, the PDMS and PU-1 coatings had hydrophobic and hydrophilic polymeric matrixes, respectively. But their ice adhesion strength did not vary considerably. This development highlights the intrinsic effect of surface roughness over ice adhesion strength regardless of the influence of wettability. In terms of CAH relevance for the pristine polymeric coatings, ice adhesion strength did not correlate with CAH as their roughnesses were lower than 0.5 µm.

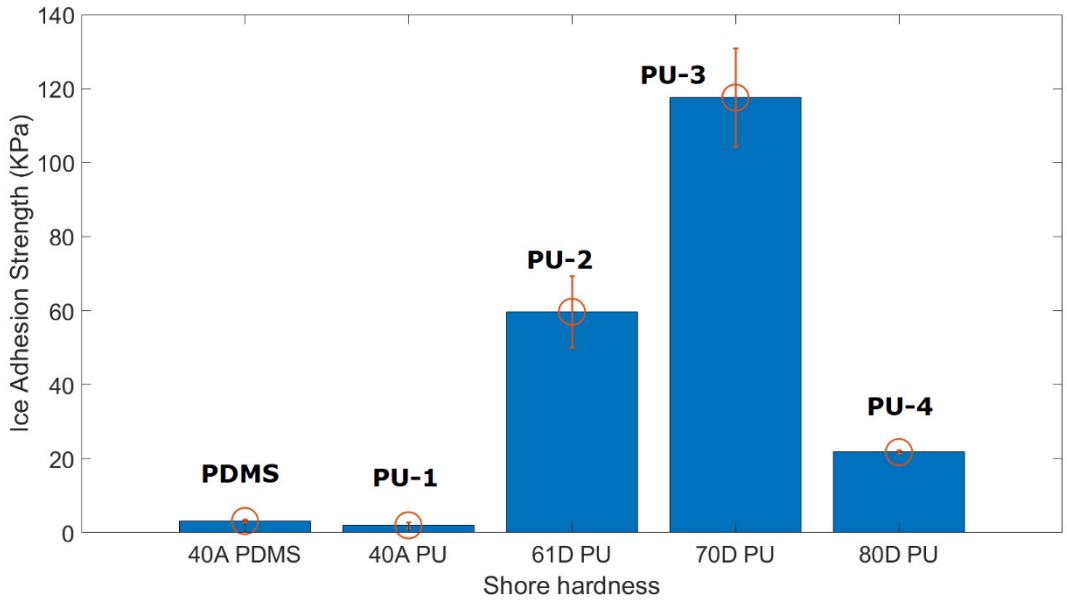

Figure 3: Ice adhesion strength versus shore hardness of pristine polymers.

Another engaging observation is the dependence of hardness of the polymeric coatings as shown in figure 3. It was reported that ice adhesion strength decreased with the decreased polymer cross-link density which corresponded to the reduction of mechanical properties of the polymers. It is a phenomenon known as inter-facial cavitation [54, 55]. As the ice forms, it would be worth looking into the formation of ice over different polymers having different hardness. From figure 4, it is suggested that the ice adhesion strength on polymeric surfaces increased as the shore hardness is increased at first. However, the ice adhesion strength is quite low on PU-4 coatings with a shore hardness of 80D. Considering PU-4 is the hardest among the developed polymers, the hardness of the polymer could be a secondary factor for

ice adhesion strength as PU-4 has lower surface roughness as compared to PU-2 and PU-3 coatings.

3.2.3.2 Polymeric nanocomposite coatings

Surface roughness of TPU-hBN coatings was controlled using the incorporation of nanoparticles in the polymer matrix. Higher amount of nanoparticles reflected the high change in surface roughness and vice versa. Again, the ice adhesion strength clearly correlated with surface roughness as indicated in figure S3.

Interestingly, the ice adhesion strength dropped drastically from TPU-60 to TPU-5 samples. However, it remained stagnant on TPU-60 and TPU-80 samples, and CAH went irrelevant. In all the cases, the effect of surface roughness was instrumental on ice adhesion strength and could not be neglected. Ice adhesion strength on TPU-80 coatings decreased from 141.22 ± 7 KPa to 25.9 ± 2 KPa on TPU-5 coatings, i.e. a 5-fold reduction.

3.2.3.3 Superhydrophobic polymeric coatings

In the previous section, we demonstrated the dependence of ice adhesion strength over surface roughness regardless of the wettability. In this section, we intend to study the effect of the surface altered from hydrophobic to superhydrophobic (with the same material composition) as shown in figure 4. SHS-5 was a hydrophobic coating and ice adhesion on this coating was measured to be 5.4 ± 2 KPa, mainly due to the effect of inter-facial cavitation as mentioned in sub-section 3.2.3. SHS-5/SHS-10/SHS-20 were superhydrophobic coatings and their ice adhesion strengths increased as the concentration of SiO_2 nanoparticles in the polymer matrix were increased.

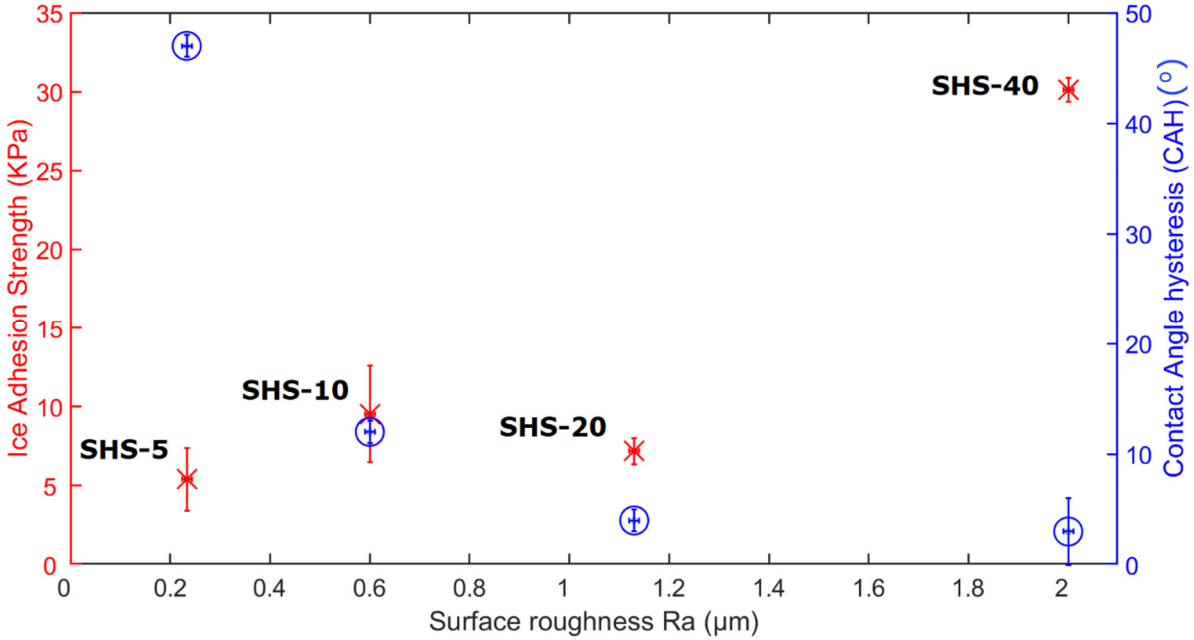

Figure 4: Ice adhesion strength versus surface roughness of superhydrophobic coatings.

Five key points of view can be drawn from these results. Firstly, when the wettability of PDMS-nSiO_2 coatings was tuned from hydrophobicity to superhydrophobicity, there was no significant change in ice adhesion strength. This could be the result of either the hardening of nanocomposite coatings drive the ice adhesion strength up or the anchoring points for the ice were enhanced. Secondly, the ice adhesion strengths on SHS-10 and SHS-20 tend to remain in the same range which gives the idea that the superhydrophobicity induced icephobicity was imparted to the coatings. Superhydrophobicity induced icephobicity is basically icephobicity achieved using minimal contact with surface asperities which results in less influence of surface properties (heterogeneous ice nucleation) and disrupts heat exchange between ice and the surface which leads to weakly bonded ice (discouragement of solidification frontier formation). Thirdly, the surface roughness becomes a dominant factor in SHS-40 coatings and the anchoring (mechanical interlocking of ice) was imminent. Fourthly, the surface roughness remained a considerable factor in all the results and followed

suit along with other hydrophobic and hydrophilic coatings/substrates. Lastly, CAH showed no direct relationship to reduce the ice adhesion strength for PDMS-nSiO_2 coatings.

3.3 Overview of the influence of surface roughness on ice adhesion strength

Ice adhesion strength versus variable surface roughness discussed in section 3.2 is summarized in figure 5. Overall, the ice adhesion strength tends to decrease with the reduction in surface roughness values. Ice adhesion strength above 160 KPa could not be determined due to the equipment limitation. However, there is sufficient evidence in the available literature of increased ice adhesion strength beyond 160 KPa with an increase in surface roughness. Momen et al. [20] reported ice adhesion strengths of 220 KPa and 270 KPa at Ra values of 5 µm and 8 µm respectively, using a similar centrifugal method. Another study involving blade de-icing under centrifugal influence reported a 250% increase in ice adhesion strength, i.e. ~200 KPa to ~670 KPa on samples with a surface roughness Ra of 0.65 µm to 2.67 µm, respectively [56]. Hassan et al. [57] found a linear correlation on samples having surface roughness Ra of 0.47 to 1.65 µm and ice adhesion strength of 142 KPa to 2279 KPa.

The lowest surface roughness in figure 5 corresponds to SS-S3 substrates. However, PU-1 coatings have the lowest ice adhesion strength among the studied surfaces. This signifies the collective or synergetic effect of surface properties such as surface energy or inter-facial cavitation that affect icephobic performance. The ice adhesion strength test was conducted based on bulk ice accretion (glaze ice) and it would be worthwhile to look into different methods such as impact ice (in-cloud ice) and hard rime ice (precipitated ice). A recent study that suggested higher ice adhesion strength may occur in these methods [58]. The data in figure 5 can also be categorized into two groups: one is hydrophobic and hydrophilic coatings and the other is superhydrophobicity induced icephobic coatings. Although ice adhesion

strength on both coating groups has a correlation with surface roughness, superhydrophobic coatings tend to be rougher in comparison to other coatings and maintain promising icephobic performance in high roughness ranges and showed no correlation with CAH. This can be justified as superhydrophobicity induced icephobicity is mainly achieved by reducing the cross-sectional area of water contact, thus the effect of surface roughness is minimal but evident.

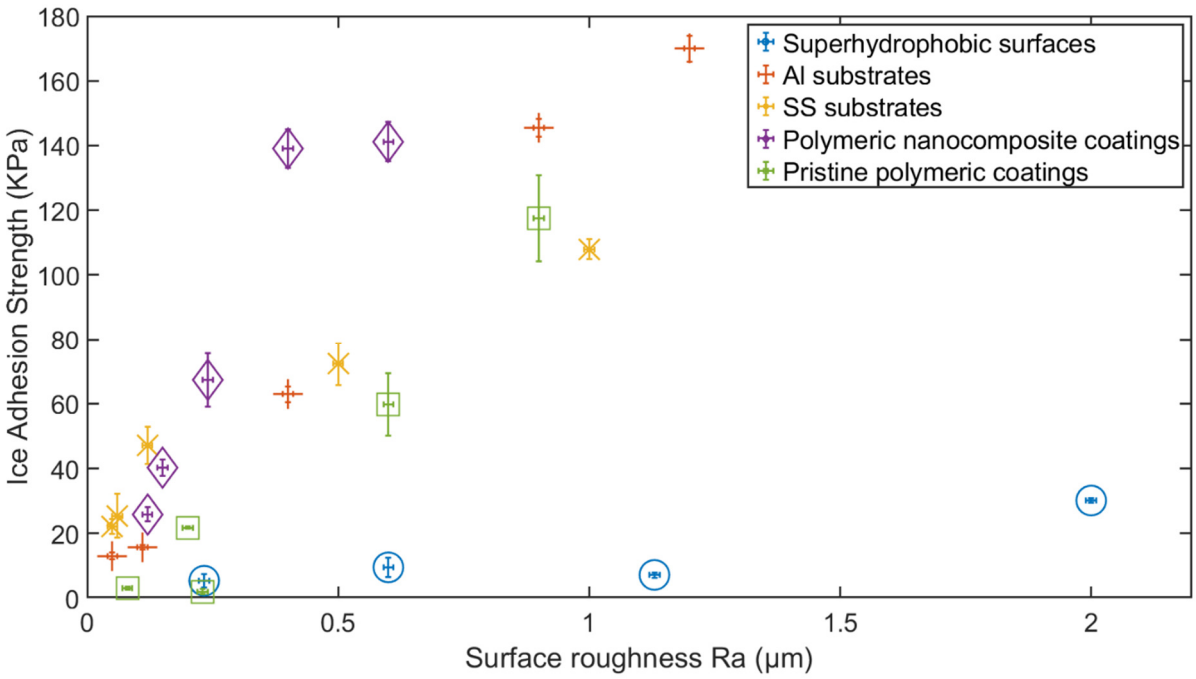

Figure 5: Overview of ice adhesion strength versus variable surface roughnesses.

3.4 Influence of surface energy on ice adhesion strength

We have so far justified the influence of surface roughness on ice adhesion strength. However, we did not explicitly check the influence of surface energy with similar surface roughness. Al-fSB/SS-fSB and TPU-f5 were functionalized using POTS via chemical vapor deposition and nanoparticle functionalization, respectively. Substrates/coatings were developed with similar surface roughness (± 0.05 µm) and identical samples were used for

WCA and ice adhesion strength tests (three samples each) to avoid the degradation of POTS layers due to hydrolysis [59].

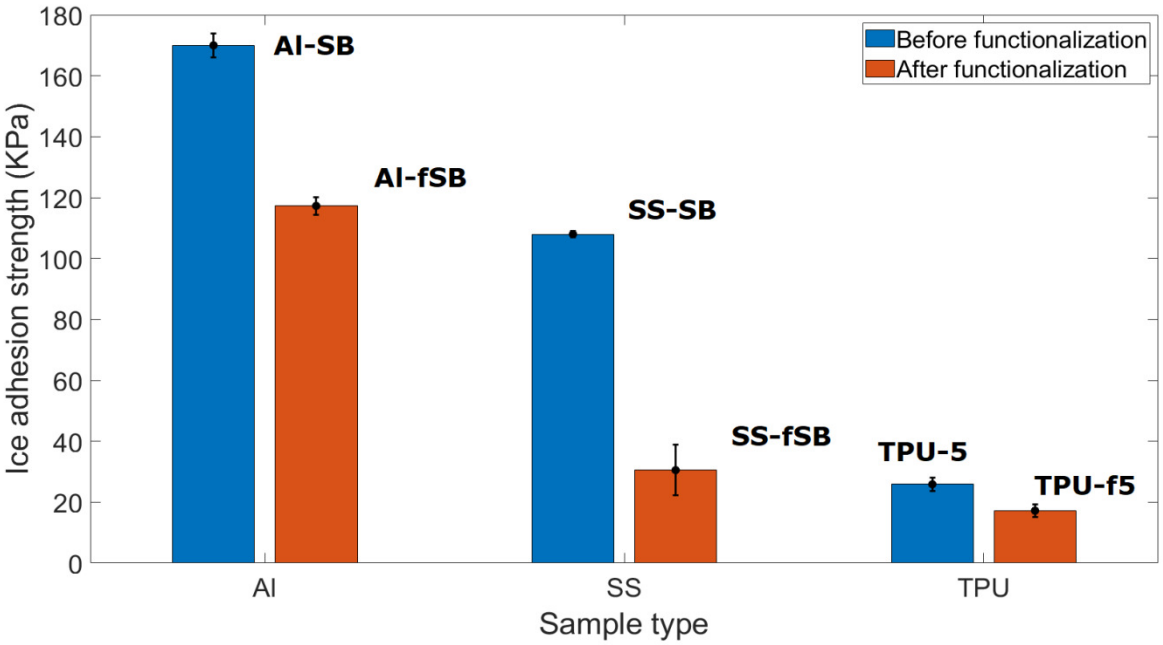

Figure 6: Ice adhesion strength: application of low surface energy chemical.

The ice adhesion strength results indicated that the introduction of low surface energy on the surfaces aided the easy removal of ice and resulted in lower shear strength, compared to the non-functionalized surface as indicated in figure 6. It is imperative to mention that the introduction of a low surface energy chemical on the surface rendered the surface hydrophobic but no significant change in receding angles was observed. These results are in conflict with other studies [14, 25, 46, 60] which indicated the influential and direct proportional roles of receding angles on ice adhesion strength. Zou et al. [5] reported the reduction of ice adhesion strength on functionalized surfaces having similar surface roughness and nearly doubled ice adhesion strength on sandblasted aluminium substrates as compared to bare aluminium substrates. This study correlated well with our results. The application of the low surface energy treatment resulted in an average decrease of 47% in ice adhesion strength across the tested surfaces.

4 In-situ icing studies

Based on the discussion above, we have thoroughly explained the influence of surface roughness on the ice adhesion strength and how it changes with the introduction of low surface energy treatment. Furthermore, it would be interesting to observe the visualization of the ice anchoring process. In this section, in-situ icing observation was conducted on Al-AR, Al-S3, SS-AR, SS-S3, SHS-40, and TPU-10BN surfaces. The surfaces were carefully selected to consider the effect of surface roughness. The ice was nucleated at high humidity conditions (90-98% RH) under low-pressure on a cold Peltier stage (-8 ºC to -3 ºC). Ice was formed on the studied surfaces at different temperatures as the thermal gradient across the observed surfaces changed. Similar technique was also employed in other studies, and in-situ ice growth (growth of water droplets in the void valley) was confirmed on superhydrophobic surfaces [61-63]. Above mentioned conditions also set to induce capillary action of water droplets among the surface grooves and the ice would form in and around the surface rough asperities. This icing condition would nullify the effect of superhydrophobic surfaces by inducing micro-condensation and forming a thin layer of ice. The formed in-situ ice was retracted at higher temperatures (above the freezing temperature on the top surface) and lower humidity levels (60-80% RH) to ensure controlled receding of the ice.

4.1 Al-AR and SS-AR surfaces

The ice retraction process on Al-AR substrates is depicted in figure 7 (a-f). Figure 7a illustrates the direction of the retraction and figure 7b shows the weakening of the ice and fragmentation of the ice into smaller sections. Retracted ice is clearly indicated in figure 7c, 7d, 7e, and 7f, and the ice anchoring is evident throughout the ice retraction process.

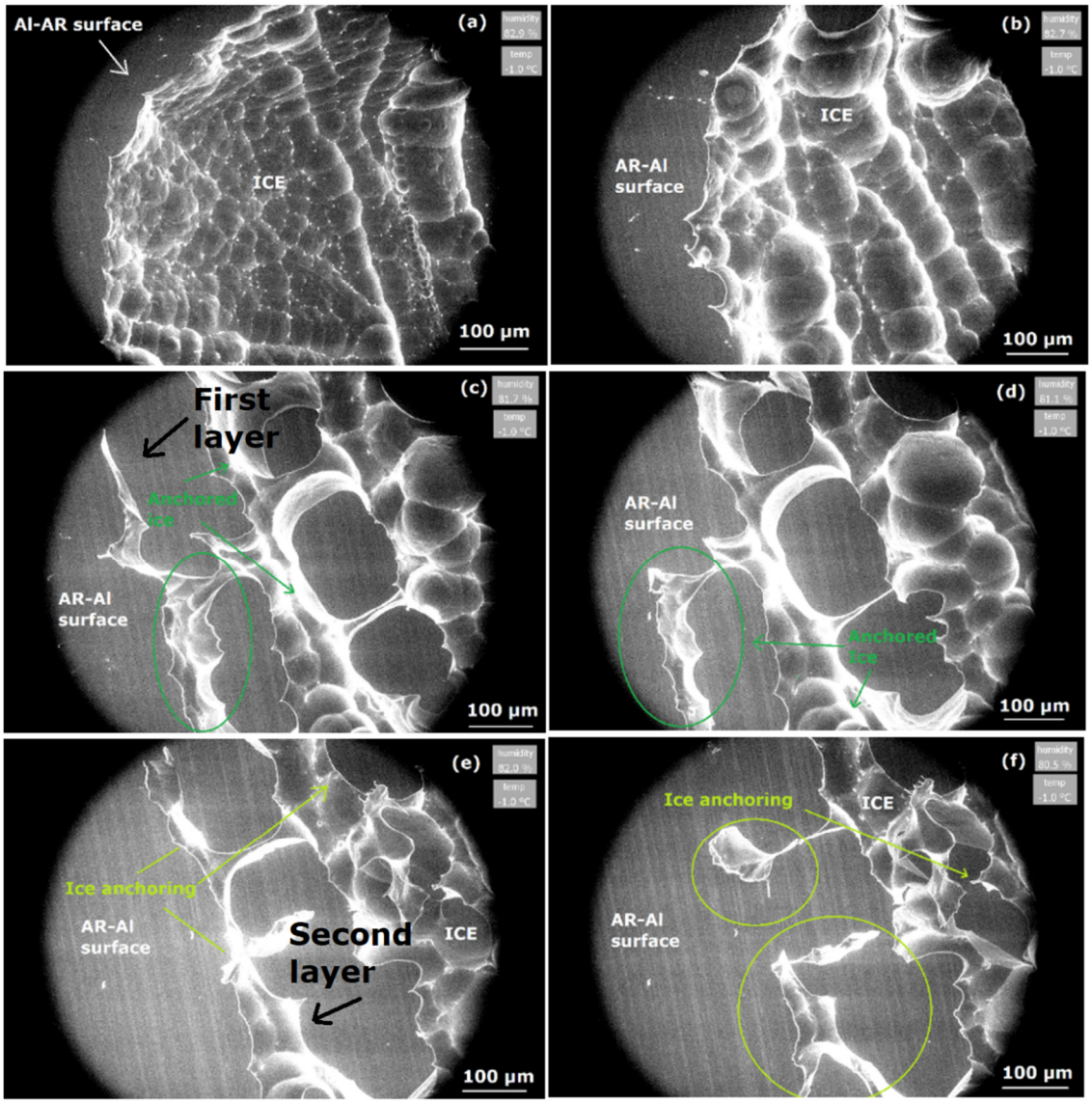

Figure 7: In-situ icing retraction on Al-AR samples after (a) 0, (b) 20, (c) 60, (d) 80, (e) 140, and (f) 160 seconds.

As the retraction process continues in figure 7c, the ice starts to break into segments and shows early signs of anchored ice. Anchoring of ice is clearly observed in figure 7d even after the 80 seconds of the ice retraction process. Finally, the initial anchored ice is fully retracted (figure 7e), and the ice anchoring is maintained in the second layer of block ice. The ice anchoring mechanism is fully validated in figure 7f, when the second layer of ice anchoring is completely detached from the main ice block and the second layer of ice continues to remain anchored on the surface as indicated (circled) in figure 7f. It is

imperative to mention that the micro-sized ice in the surface rough grooves provides anchoring points of the ice to strongly adhere to the surface and the ice adhesion strength would be significantly higher. Similar behavior was observed on SS-AR substrates, but the ice anchoring was less severe compared to Al-AR, owing to the difference in material composition as well as the surface roughness.

4.2 Al-S3 and SS-S3 surfaces

In comparison to the as-received substrates, SS-S3 substrates were deployed for the in-situ icing study and the ice was formed uniformly throughout the observed surface. Interestingly, there is no ice anchoring present on the smoothened substrates as evidenced in figure 8.

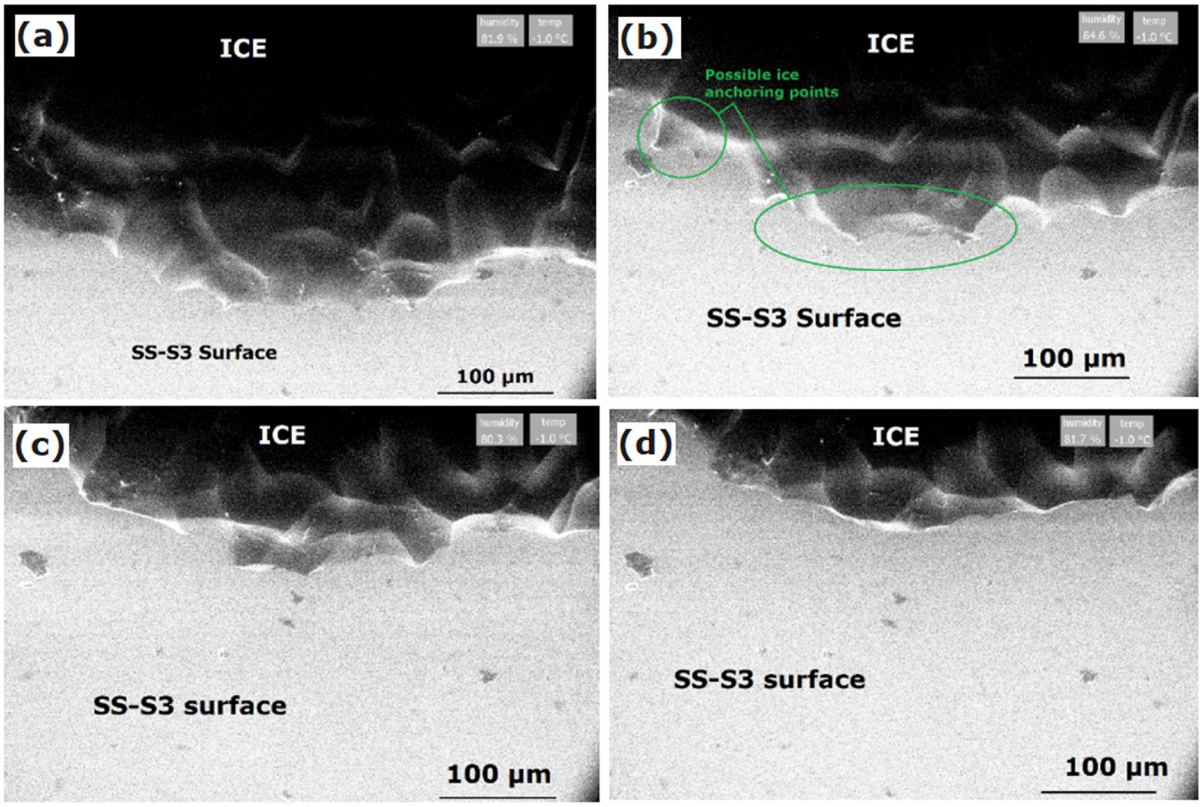

Figure 8: In-situ icing retraction on SS-S3 samples after (a) 0, (b) 40, (c) 60, and (d) 80 seconds.

Uniform formation of ice can be observed in figure 8a, and the possible ice anchoring points/sites are identified in figure 8b. In figure 8c, the ice retracts and does not anchor as

previously noted on the as-received substrates. Ice continues to retract without anchoring as indicated in figure 8d. These are promising results as it visualizes the effect of surface roughness and highlights its importance on ice adhesion strength which indicates a similar correlation. These studies validate the effect of micro-condensation on ice adhesion strength and subsequently on icephobic performance.

4.3 Superhydrophobic surfaces

SHS-40 had a superhydrophobic surface and the ice anchoring mechanism was evident. The ice anchoring was severe and the effect of this ice anchoring was also verified from ice adhesion strength as its ice adhesion strength raised 5.4 times as compared to the SHS-5 surface.

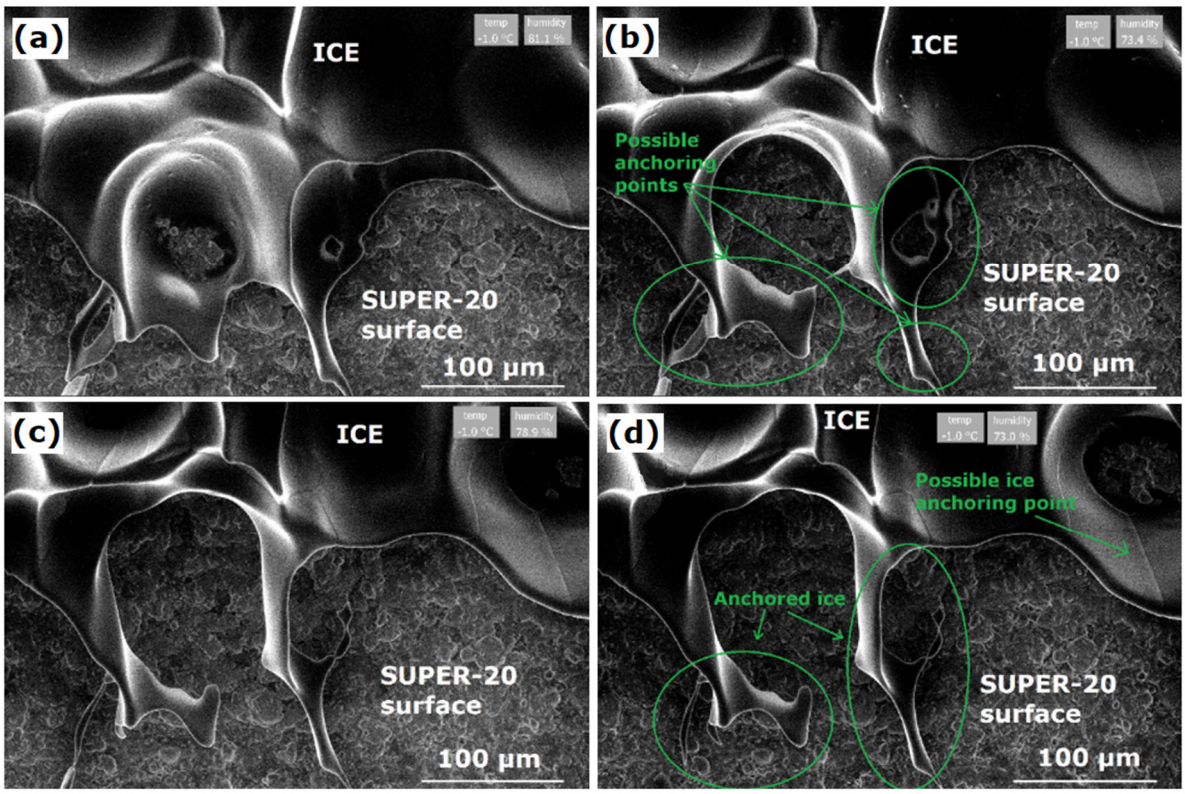

Figure 9: In-situ icing retraction on SHS-40 samples after (a) 0, (b) 40, (c) 60, and (d) 80 seconds.

In figure 9a, the ice anchoring is developing vigorously and the possible ice anchoring points are marked in figure 9b. Developed ice remains even after 80 seconds of ice retraction process as observed in figure 9c, and stubborn ice anchoring is observed on these surfaces as illustrated in figure 9d. The size of the anchor was considerably large in size (10-30 µm) and was comparable to Al-AR substrates in section 4.1. Preliminary results suggest that the superhydrophobicity of the surface neither had a mitigating effect on the level of anchoring nor it prevented the anchoring to occur.

4.4 Polymeric nanocomposite coatings

The ice retraction process on the TPU-10BN surface narrated a significantly different concept, as shown in figure 10. In figure 10a, instead of retracting outward towards the edge of the coating (as observed on other coatings/surfaces), the ice simply started the melting at the accretion positions. In figure 10b, the ice was melting in fragmented sections and smaller patches of ice were anchored on the surface as indicated. These patches of ice became more visible in figure 10c, and these patches stayed on the observed surface even after the big blocks of ice were completely melted (figure 10d). These results depicted the intense and stubborn ice anchoring mechanism. In comparison to the ice adhesion strength results, TPU-10BN did not show higher ice adhesion strength which signified the effect of inter-facial cavitation and the ice detaches due to the soft nature of the polymer matrix.

Furthermore, as the concentration of BN particles increased in the TPU-BN nanocomposites, the ice adhesion strength of these nanocomposites nearly equated that measured on the SS-AR substrates. Thus, it could be assumed that the inter-facial cavitation became less effective with the hardening of the polymer. The possible assumption of this significant increase in ice adhesion strength is the severity of ice anchoring observed on TPU-BN nanocomposites which leads to a stronger ice bond on the surface.

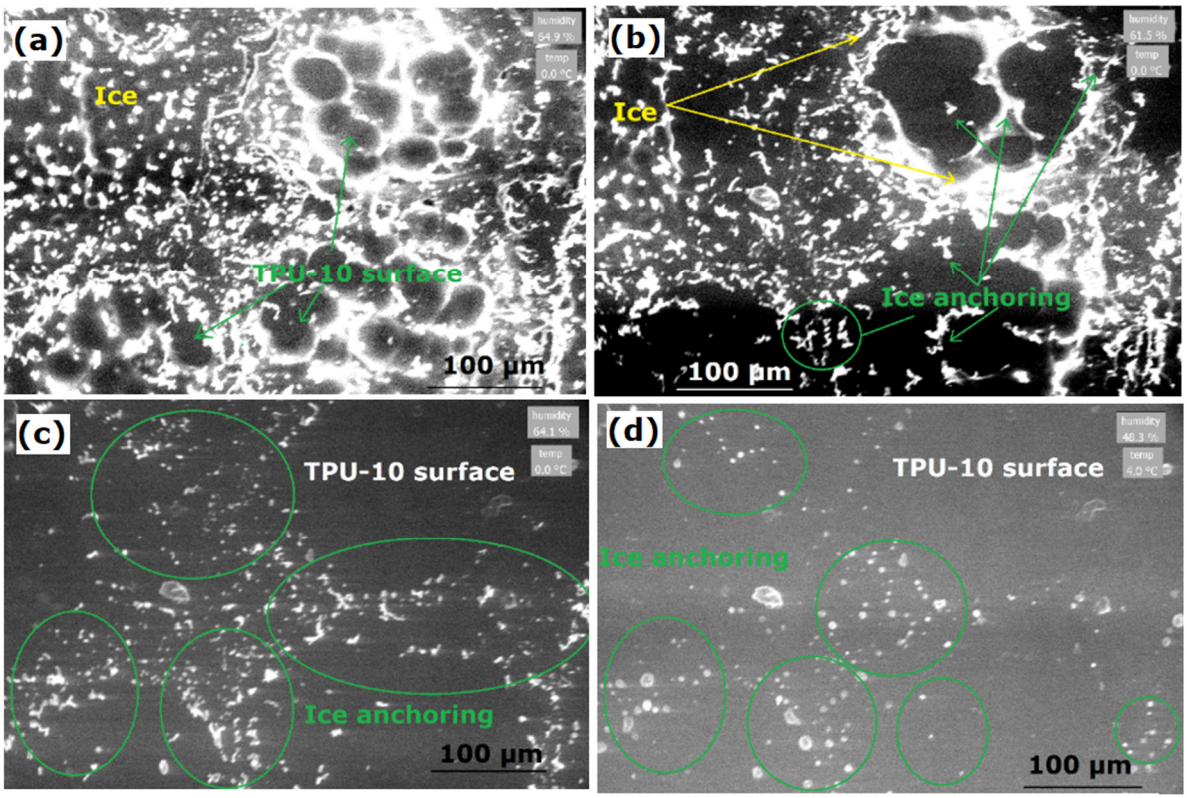

Figure 10: In-situ icing retraction on TPU-10BN samples after (a) 0, (b) 40, (c) 60, and (d) 80 seconds.

5 Conclusions

Surface roughness and superhydrophobicity have been long debated for inducing icephobicity and contradictory results were reported in anti-icing and de-icing applications. In this work, the systematic reduction of ice adhesion strength was demonstrated with the decrease of surface roughness regardless of surface wettability.

On metallic surfaces, ice adhesion strength was reduced dramatically by lowering the surface roughness, without any surface coating and functionalization. For aluminium specimens, surface roughness was reduced by 24-fold which resulted in an 11-fold or ~91% reduction in ice adhesion strength. Ice adhesion strength on polymeric coatings also decreased with a decrease in surface roughness. Superhydrophobicity-induced icephobicity was evident on PDMS-nSiO_2 coatings, but with a higher concentration of functionalized silicon dioxide

nanoparticles in the PDMS matrix, ice adhesion strength surged mainly due to the increase in the surface roughness.

These results were further validated by deploying in-situ icing study and ice did not anchor on smoothened metallic surfaces but anchored on the as-received metallic surfaces and polymeric coatings. Surface wettability did not correlate with ice adhesion strength based on our results. The studied PDMS and PU coatings are hydrophobic and hydrophilic, respectively. However, their ice adhesion strengths did not change considerably. On the contrary, low surface energy treatment on the surface showed a direct reduction of ice adhesion strength. These results signify the synergetic effect of surface roughness and surface energy on ice adhesion strength (in line with the interfacial correlation factor) as the developed pristine polymers were comparably smooth. Furthermore, the functionalization of surfaces with low surface energy layer would not be confused with the wettability as no significant changes in receding angles were observed on the treated coatings. Additionally, it is imperative to mention that the superhydrophobic coatings demonstrated a reduction in contact angle hysteresis as the concentration of functionalized silicon dioxide nanoparticles increased but there was no clear reduction in ice adhesion strength (in correlation with CAH) as debated in the available literature. Interestingly, CAHs of all the studied surfaces (except pristine polymeric and superhydrophobic coatings) demonstrated a strong correlation with ice adhesion strength below the surface roughness of R_a 0.4 µm.

Acknowledgment

This work was supported by the studentship from Faculty of Engineering, University of Nottingham and has partially received funding from the CleanSky 2 Joint Undertaking under the European Union's Horizon 2020 research and innovation programme under grant agreement No CS2-AIR-GAM-2014-2015-O1. Cf. Art.29.4 of [A2]. The authors also thank

Dr. Barbara Turnbull for helping with ice adhesion strength test and acknowledge the use of facilities at Nanoscale and Microscale Research Centre of the University of Nottingham supported by Engineering and Physical Sciences Research Council [grant number EP/L022494/1].

References

[1] A.B.D Cassie, S. Baxter, Transactions of the Faraday society, 40 (1944) 546-551.

[2] S. Herminghaus, EPL (Europhysics Letters), 52 (2000) 165.

[3] D. Öner, T.J. McCarthy, Langmuir, 16 (2000) 7777-7782.

[4] Z. Yoshimitsu, A. Nakajima, T. Watanabe, K. Hashimoto, Langmuir, 18 (2002) 5818-5822.

[5] M. Zou, S. Beckford, R. Wei, C. Ellis, G. Hatton, M.A. Miller, Applied Surface Science, 257 (2011) 3786-3792.

[6] P. Tourkine, M. Le Merrer, D. Quéré, Langmuir, 25 (2009) 7214-7216.

[7] A. Alizadeh, M. Yamada, R. Li, W. Shang, S. Otta, S. Zhong, L. Ge, A. Dhinojwala, K.R. Conway, V. Bahadur, A.J. Vinciquerra, Langmuir, 28 (2012) 3180-3186.

[8] V. Bahadur, L. Mishchenko, B. Hatton, J.A. Taylor, J. Aizenberg, T. Krupenkin, Langmuir, 27 (2011) 14143-14150.

[9] L. Mishchenko, B. Hatton, V. Bahadur, J.A. Taylor, T. Krupenkin, J. Aizenberg, ACS Nano, 4 (2010) 7699-7707.

[10] G. Fang, A. Amirfazli, Surface Innovations, 2 (2014) 94-102.

[11] Y. Wang, J. Xue, Q. Wang, Q. Chen, J. Ding, ACS Appl. Mater. Interfaces, 5 (2013) 3370-3381.

[12] Y. Shen, H. Tao, S. Chen, L. Zhu, T. Wang, J. Tao, RSC Adv., 5 (2015) 1666-1672.

[13] G. Momen, M. Farzaneh, Applied Surface Science, 299 (2014) 41-46.

[14] S.A. Kulinich, M. Farzaneh, Langmuir, 25 (2009) 8854-8856.

[15] A.J. Meuler, G.H. McKinley, R.E. Cohen, ACS Nano, 4 (2010) 7048-7052.

[16] Y. Wang, M. Li, T. Lv, Q. Wang, Q. Chen, J. Ding, Journal of Materials Chemistry A, 3 (2015) 4967-4975.

[17] Y.H. Yeong, A. Steele, E. Loth, I. Bayer, G. De Combarieu, C. Lakeman, Appl. Phys. Lett., 100 (2012) 053112.

[18] X. Sun, V.G. Damle, S. Liu, K. Rykaczewski, Advanced Materials Interfaces, 2 (2015) 1400479.

[19] S.A. Kulinich, S. Farhadi, K. Nose, X.W. Du, Langmuir, 27 (2010) 25-29.

[20] G. Momen, R. Jafari, M. Farzaneh, Applied Surface Science, 349 (2015) 211-218.

[21] R. Karmouch, G.G. Ross, J. Phys. Chem. C, 114 (2010) 4063-4066.

514 [22] T. Wang, Y. Zheng, A.R.O. Raji, Y. Li, W.K. Sikkema, J.M. Tour, ACS Appl. Mater.
515 Interfaces, 8 (2016) 14169-14173.

516 [23] P. Kim, T.S. Wong, J. Alvarenga, M.J. Kreder, W.E. Adorno-Martinez, J. Aizenberg,
517 ACS Nano, 6 (2012) 6569-6577.

518 [24] K.K. Varanasi, T. Deng, J.D. Smith, M. Hsu, N. Bhate, Applied Physics Letters, 97
519 (2010) 234102.

520 [25] M. Nosonovsky, V. Hejazi, ACS Nano, 6 (2012) 8488-8491.

521 [26] R.N. Ben, ChemBioChem, 2 (2001) 161-166.

522 [27] J.G. Smith, C.J. Wohl, R.E. Kreeger, J. Palacios, T. Knuth, in: 8th AIAA Atmospheric
523 and Space Environments Conference, 2016, pp. 3444.

524 [28] H. Zhu, Z. Guo, W. Liu, Chemical Communications, 50 (2014) 3900-3913.

525 [29] S.L. Sivas, B. Riegler, R. Thomaier, K. Hoover, in: 39th International Society for the
526 Advancement of Materials and Process Engineering Technical Conference, 2007, pp. 53-58.

527 [30] H. Zheng, S. Chang, Y. Zhao, Progress in Chemistry, 29 (2017) 102-118.

528 [31] S. Ozbay, H.Y. Erbil, Colloids and Surfaces A: Physicochemical and Engineering
529 Aspects, 504 (2016) 210-218.

530 [32] J. Chen, Z. Luo, Q. Fan, J. Lv, J. Wang, Small, 10 (2014) 4693-4699.

531 [33] T.M. Schutzius, S. Jung, T. Maitra, P. Eberle, C. Antonini, C. Stamatopoulos, D.
532 Poulikakos, Langmuir, 31 (2015) 4807-4821.

533 [34] P. Hao, C. Lv, X. Zhang, Appl. Phys. Lett., 104 (2014) 161609.

534 [35] J. Seyfi, S.H. Jafari, H.A. Khonakdar, G.M.M. Sadeghi, G. Zohuri, I. Hejazi, F. Simon,
535 Applied Surface Science, 347 (2015) 224-230.

536 [36] S. Jung, M. Dorrestijn, D. Raps, A. Das, C.M. Megaridis, D. Poulikakos, Langmuir, 27
537 (2011) 3059-3066.

538 [37] L. Cao, A.K. Jones, V.K. Sikka, J. Wu, D. Gao, Langmuir, 25 (2009) 12444-12448.

539 [38] P. Eberle, M.K. Tiwari, T. Maitra, D. Poulikakos, Nanoscale, 6 (2014) 4874-4881.

540 [39] X.Y. Liu, J. Phys. Chem. B, 105 (2001) 11550-11558.

541 [40] X.Y. Liu, K. Maiwa, K. Tsukamoto, J. Chem. Phys., 106 (1997) 1870-1879.

542 [41] Z. Zhang, X.Y. Liu, Chemical Society Reviews, 47 (2018) 7116-7139.

543 [42] G. Heydari, E. Thormann, M. Järn, E. Tyrode, P.M. Claesson, The Journal of Physical
544 Chemistry C, 117 (2013) 21752-21762.

545 [43] N.H.J Fletcher, The Journal of chemical physics, 29 (1958) 572-576.

546 [44] H. Memon, J. Liu, N. Weston, J. Wang, D. De Focatiis, K.S. Choi, X. Hou, Cold
547 Regions Science and Technology, (2019) 102814.

548 [45] J. Liu, J. Wang, H. Memon, Y. Fu, T. Barman, K.S. Choi, X. Hou, Surface and Coatings
549 Technology, 357 (2019) 267-272.

550 [46] Z.A. Janjua, B. Turnbull, K.L. Choy, C. Pandis, J. Liu, X. Hou, K.S. Choi, Applied
551 Surface Science, 407 (2017) 555-564.

552 [47] S.A. Kulinich, M. Farzaneh, Applied Surface Science, 255 (2009) 8153-8157.

553 [48] C. Laforte, A. Beisswenger, in: Proceedings of the 11th International Workshop on
554 Atmospheric Icing of Structures, IWAIS, Montreal, QC, Canada, 2005, pp. 12-16.

555 [49] S. Rønneberg, Y. Zhuo, C. Laforte, J. He, Z. Zhang, Coatings, 9 (2019) 678.

556 [50] S. Rønneberg, J. He, Z. Zhang, Journal of Adhesion Science and Technology, (2019) 1-
557 29.

558 [51] L. Boinovich, A.M. Emelyanenko, Langmuir, 30 (2014) 12596-12601.

559 [52] R. Jafari, R. Menini, M. Farzaneh, Applied Surface Science, 257 (2010) 1540-1543.

560 [53] F. Arianpour, M. Farzaneh, International Journal of Theoretical and Applied
561 Nanotechnology, 1 (2012) 79-85.

562 [54] K. Golovin, S.P. Kobaku, D.H. Lee, E.T. DiLoreto, J.M. Mabry, A. Tuteja, Sci. Adv., 2
563 (2016) e1501496.

564 [55] C. Wang, T. Fuller, W. Zhang, K.J. Wynne, Langmuir, 30 (2014) 12819-12826.

565 [56] J. Soltis, J. Palacios, T. Eden, D. Wolfe, AIAA journal, 53 (2014) 1825-1835.

566 [57] M.F. Hassan, H.P. Lee, S.P. Lim, Measurement Science and Technology, 21 (2010)
567 075701.

568 [58] S. Rønneberg, C. Laforte, C. Volat, J. He, Z. Zhang, AIP Advances, 9 (2019) 055304.

569 [59] S.A. Kulinich, M. Honda, A.L. Zhu, A.G. Rozhin, X.W. Du, Soft Matter, 11 (2015) 856-
570 861.

571 [60] A.J. Meuler, J.D. Smith, K.K. Varanasi, J.M. Mabry, G.H. McKinley, R.E. Cohen, ACS
572 Appl. Mater. Interfaces, 2 (2010) 3100-3110.

573 [61] L.B. Boinovich, A.M. Emelyanenko, K.A. Emelyanenko, E.B. Modin, ACS Nano, 13
574 (2019) 4335-4346.

575 [62] C.S. Sharma, J. Combe, M. Giger, T. Emmerich, D. Poulikakos, ACS Nano, 11 (2017)
576 1673-1682.

577 [63] T. Maitra, S. Jung, M.E. Giger, V. Kandrical, T. Ruesch, D. Poulikakos, Advanced
578 Materials Interfaces, 2 (2015) 1500330.
579

580 List of Figures